Bioorg. Med. Chem. 143 (2026) 118794

Contents lists available at ScienceDirect

Bioorganic & Medicinal Chemistry

journal homepage: www.elsevier.com/locate/bmc

Structure-based design of a 1*H*-Tetrazole-containing scaffold for Caspase-1 inhibition: Synthesis, biological evaluation, and preliminary in Vivo studies

Ajay L. Chandgude [a], Giovanni Loriga [b], Andrea Beccu [b], Fabio Arturo Iannotti [c], Ester Pagano [d], Raffaele Capasso [e], Riccardo Fusco [f,g], Pietro Spanu [b,*,h], Fausta Ulgheri [b,h], Alexander Domling [a,f,g,h]

[a] *Department of Drug Design, University of Groningen, the Netherlands*
[b] *Institute of Biomolecular Chemistry, National Research Council (CNR), Trav. La Crucca 3, 07100 Sassari, Italy*
[c] *Institute of Biomolecular Chemistry, National Research Council (CNR), Via Campi Flegrei 34, 80078 Pozzuoli, NA, Italy*
[d] *Department of Pharmacy, University of Naples Federico II, 80131 Naples, Italy*
[e] *Department of Agricultural Sciences, University of Naples Federico II, Portici 80055, Italy*
[f] *Czech Advanced Technology and Research Institute (CATRIN), Palacký University Olomouc, Slechtitelů 27, 77900, Olomouc, Czech Republic*
[g] *Institute of Molecular and Translational Medicine, Faculty of Medicine and Dentistry, Palacký University and University Hospital Olomouc, Hněvotínská 1333/5, Olomouc 77900, Czech Republic.*

ARTICLE INFO

Keywords:
Caspase-1
Inflammasome
1*H*-Tetrazoles
Multicomponent reactions
Duchenne muscular dystrophy

ABSTRACT

Targeting caspase-1 with small-molecule inhibitors represents a promising strategy for the treatment of inflammatory diseases. Herein, we report the structure-based design, synthesis, and biological evaluation of a new 1*H*-tetrazole-containing scaffold for caspase-1 inhibitors. This scaffold incorporates a 1*H*-tetrazole as a carboxylic acid bioisostere and lacks electrophilic functionalities commonly employed to promote covalent modification of the catalytic cysteine. The resulting molecules inhibited caspase-1 with IC_{50} values ranging from the mid-nanomolar to low-micromolar range, with compounds **6e** and **6f** emerging as the most potent inhibitors (IC_{50} = 380 and 360 nM, respectively). Compared with our previously reported 1,5-disubstituted α-aminotetrazole series, compounds **6e** and **6f** showed an approximately 30-fold improvement in enzymatic potency. Preliminary in vivo evaluation of compound **6e** in a dystrophic mouse model suggested a trend toward improved muscle coordination and strength, while no toxicity was observed in murine muscle cells under the tested conditions. Molecular dynamics simulations suggested different binding behaviors, conformational preferences, and interaction patterns for the two enantiomers of compound **6e** within the caspase-1 binding pocket. Overall, this work broadens the structural diversity of tetrazole-based caspase-1 inhibitors by introducing a distinct 1*H*-tetrazole-containing scaffold with enhanced caspase-1 inhibitory activity and provides a promising starting point for further optimization.

1. Introduction

The innate immune system provides the first line of defense against pathogens and homeostatic perturbations in multicellular organisms. A central mechanism of innate immune responses is the activation of inflammasomes, cytosolic multiprotein complexes assembled in response to endogenous or pathogen-derived stimuli that promote the maturation of pro-inflammatory cytokines and induce pyroptosis through caspase-1 activation.[1,2] This response enables rapid and broad protection against infection and stress and contributes to the activation of adaptive immunity. In addition, inflammasomes are integral components of the recently described PANoptosome, a higher-order signaling complex that regulates PANoptosis, a coordinated inflammatory cell death program integrating pyroptosis and other cell death pathways to eliminate infected or damaged cells.[3]

Given their central role in host defense, inflammasome activation must be tightly regulated to prevent tissue damage. Dysregulated activation, leading to excessive release of inflammatory mediators and

* Corresponding author.
E-mail address: pietro.spanu@cnr.it (P. Spanu).
[h] These authors share last authorship

https://doi.org/10.1016/j.bmc.2026.118794
Received 13 July 2026; Received in revised form 26 August 2026; Accepted 31 August 2026
Available online 2 September 2026

aberrant cell death pathways, has been implicated in a wide range of pathological conditions, including autoimmune and inflammatory disorders, cytokine storm syndromes, cancer, neurodegeneration, and metabolic diseases.[4–7] Caspase-1 is a key effector of inflammasome signaling and a central regulator of innate immunity. It is activated upon inflammasome assembly and processes the inactive precursors of IL-1β, IL-18, and Gasdermin D into their active forms, thereby driving inflammatory responses.[8] Aberrant caspase-1 activation has been associated with multiple diseases, including psoriasis, arthritis, metabolic disorders, cardiovascular and neurological diseases, and Duchenne muscular dystrophy.[9–21] Accordingly, pharmacological inhibition of caspase-1 has shown protective effects in various preclinical disease models, highlighting its potential as a therapeutic target.[22–28] Despite significant efforts, the clinical translation of caspase-1 inhibitors has been limited. Only a few candidates have reached clinical evaluation, where they ultimately failed due to safety and toxicity concerns (Fig. 1).[22,29–31] Many of these compounds are covalent inhibitors, which, while often potent in vitro, frequently suffer from poor selectivity and unfavorable pharmacological properties, limiting their clinical development.[31] Despite these advances, the development of structurally diverse and pharmacologically optimized caspase-1 inhibitors remains an ongoing challenge. Structure-based computational approaches have become valuable tools in modern medicinal chemistry, supporting molecular recognition studies, scaffold optimization, and the rational interpretation of protein–ligand interactions. Molecular docking can provide structural hypotheses on ligand binding modes, while molecular dynamics simulations offer complementary insights into protein flexibility and the dynamic behavior of protein–ligand complexes. Recent advances in artificial intelligence, including structure-prediction methods such as AlphaFold, have further expanded the possibilities for computer-aided drug discovery by enabling the modelling and completion of protein structures that may otherwise be difficult to obtain experimentally. When integrated with experimental medicinal chemistry, these computational approaches can facilitate the design and prioritization of novel small molecules and guide subsequent optimization.[32–34]

In this context, we recently reported 1,5-disubstituted α-amino-tetrazole caspase-1 inhibitors as a novel class of inflammasome modulators.[35] Building on this previous work and following a strategy based on scaffold diversification and bioisosteric replacement, the present study describes a structurally distinct 1*H*-tetrazole-containing scaffold. In this design, the 1*H*-tetrazole was introduced as a carboxylic acid bioisostere to explore alternative interactions within the caspase-1 active site, with the aim of expanding the chemical space of tetrazole-based caspase-1 inhibitors and improving inhibitory potency.[36]

2. Results and discussion

Due to the highly basic nature of the caspase-1 active site, defined by residues such as Arg341, Arg179, and the catalytic Cys285, most reported direct caspase-1 inhibitors incorporate an (*L*)-aspartic acid mimic bearing an electrophilic warhead at the P1 position to promote covalent modification of the catalytic cysteine residue.[37] In contrast to these covalent inhibitors, we previously reported 1,5-disubstituted α-amino-tetrazole caspase-1 inhibitors designed to avoid covalent modification of the catalytic cysteine by replacing the cleavable aspartyl moiety with a non-cleavable 4-amino-3-hydroxybutanoic acid scaffold capable of maintaining key interactions within the catalytic site while enabling structural diversification toward the P2–P4 subsites (Fig. 2 A).[35] Inspired by this non-covalent design rationale, we investigated a structurally distinct series of inhibitors in which the P1 carboxylic acid characteristic of aspartate-based caspase-1 inhibitors was replaced by a 1*H*-tetrazole bioisostere, thereby expanding the structural diversity of

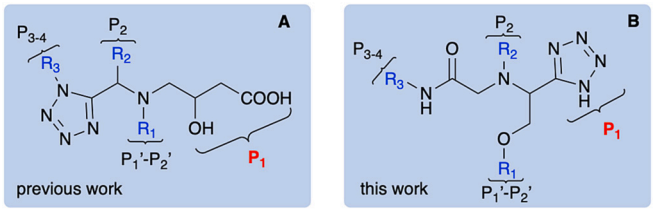

Fig. 2. Design strategy of the previously reported 1,5-disubstituted α-amino-tetrazole scaffold (A) and the present tetrazole-based scaffold (B). The substituents are shown according to their intended interactions with the P1–P4 and P1'–P2' subsites of caspase-1.

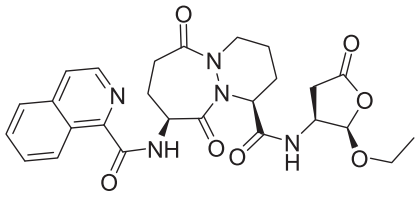

VX-740 pralnacasan (prodrug)
VRT-18858 - inhibitor of caspase-1 (K_i 1.3 nM) and LPS-induced IL-1β release in vitro PBMCs (IC_{50} 0.85 μM)

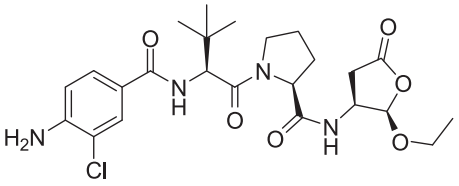

VX-765 belnacasan (prodrug)

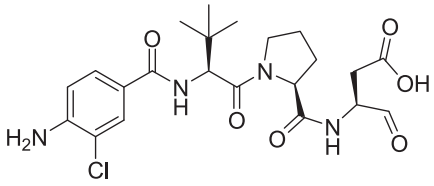

VRT-043198

VRT-043198 - inhibitor of caspase-1 (K_i 0.8 nM) and LPS-induced IL-1β release in vitro PBMCs (IC_{50} 0.47 μM)

Fig. 1. Selective caspase-1 inhibitors advanced into clinical trials but termined due to toxicity.

tetrazole-based caspase-1 inhibitors (Fig. 2B).

Compared with carboxylic acids, 1*H*-tetrazoles closely reproduce the ionization state and binding characteristics of the carboxylate while offering several potential advantages, including delocalization of the negative charge over the aromatic five-membered ring, increased lipophilicity, a more versatile hydrogen-bonding pattern, and potentially enhanced metabolic stability owing to their resistance to conjugative metabolic pathways typically associated with carboxylic acids.[38–42] Compounds prioritized through molecular modelling were synthesized by multicomponent reactions and evaluated for caspase-1 inhibitory activity. Finally, given recent evidence implicating caspase-1 activation in Duchenne muscular dystrophy, a preliminary in vivo evaluation of compound **6e** was carried out in mdx mice, the most widely used animal model of the disease.[43]

2.1. Design

Analysis of available crystal structures of caspase-1 reveals the structure of a typical protease substrate binding site, which we divide here into three main parts: the active site housing the catalytic Cys 285 and an elongated shallow channel accommodating the substrate backbone, a shallow pocket for accommodating the S2 side chain, and a remote deep cleft flanked by Trp 340, Arg 384 on one side, and His 342, Pro 343 on the other (Fig. 3A-B).

Starting with the key active site we hypothesized that the tetrazole moiety can undergo similar charge-charge and hydrogen bonding interactions to the carboxylic acid. Thus, we modeled 5-methyl-tetrazole into the active site by placing the molecule on top of the carboxylic acid moiety of a typical co-crystallized inhibitor (Fig. 3C-D). After energy minimization in the Moloc software suite we indeed found that the tetrazole could be a good starting point for caspase-1 inhibitor design. A comparison of the carboxylic acid and tetrazole moiety and the clinical caspase-1 inhibitor (Belnacasan) is shown in Fig. 3. The carboxylate of Belnacasan forms a charge-charge interaction and trifurcated hydrogen bond with the guanidine side chain of Arg 179 and Arg 341, and a hydrogen bond to the side chain amide of Gln 283. Similarly, the tetrazolate, albeit with a slightly different orientation.

We recently described synthetic methods for an acidic tetrazole moiety by employing the Ugi-tetrazole reactions (UT-4CRs).[44] This is accomplished using cleavable isocyanides, and we previously described benzyl isocyanide (hydrogen), β-cyanomethyl isocyanide (basic) or tertbutyl/1,1,3,3-tetramethylbutyl isocyanide (acidic). Ugi multicomponent reactions (U-MCR) have the great advantage of allowing to optimize several different positions in peptidomimetic scaffolds by simultaneous variation of several building blocks. Based on our experience in this chemistry we chose the UT-4CR to optimize caspase-1 inhibitors.[45]

The UT-4CR of an isocyanide, HN_3 equivalent, oxo component and a primary or secondary amine yields highly substituted tetrazole methylamines (Scheme 1).

The hypothesized binding of the overall scaffold involves the tetrazole aspartyl mimetic into the active site, R_1 into S1' pocket, R_2 next to Cys 285, and R_3 into the deep grove (Scheme 1). As an aldehyde component we chose hydroxyl acetaldehyde, to form a hydrogen bond to Gly 238 while R_1 substituent was chosen to project into the prime side S1' pocket of the enzyme (Fig. 4). To fill the S2 pocket and to extend the scaffold into the elongated shallow channel to reach the deeper groove we prepared a secondary amines component linked to several R_2 substituents and equipped with an appropriate hydrophobic R_3 substituent.

The amine R_2 substituent of the UT-4CR was chosen to fill the S2 pocket formed by Trp 340 and Val 338 (Fig. 4). Thus, we have chosen a smaller alkyl, cycloalkyl or an aromatic ring substituent to gain interaction with Trp 340. To extend the UT-4CR scaffold, a substituted phenoxy phenyl acetamido substituent was exploited. The phenyl ether part is enclosed by the narrow deep groove formed by Arg 383, Trp 360 undergoing pi-stacking interactions with the Pro 343 and His 342 on the opposite side (Fig. 4).[46]

2.2. Synthesis

To synthesize the selected tetrazole candidates in a divergent, efficient, and sustainable way, we performed UT-4CRs. As shown in Scheme 2, the reaction between secondary amines **1a-g**, commercially available aldehyde **2**, isocyanide **3**, and trimethylsilylazide **4** in methanol yielded the condensation products **5a-g** after stirring the reaction mixture at room temperature for 2–4 days. Desired products **6a-g** were obtained by the subsequent deprotection of the Ugi-products **5a-g**.

To obtain the secondary amine component required in the Ugi step linked to an alkyl, cycloalkyl or an aromatic ring substituent, amines **1b-g** were synthesized as illustrated in Scheme 3 by coupling the opportune primary amine **8b-g** to commercially available 2-chloro-*N*-(4-phenoxyphenyl) acetamide **7.** The amine **1a** was instead commercially available.

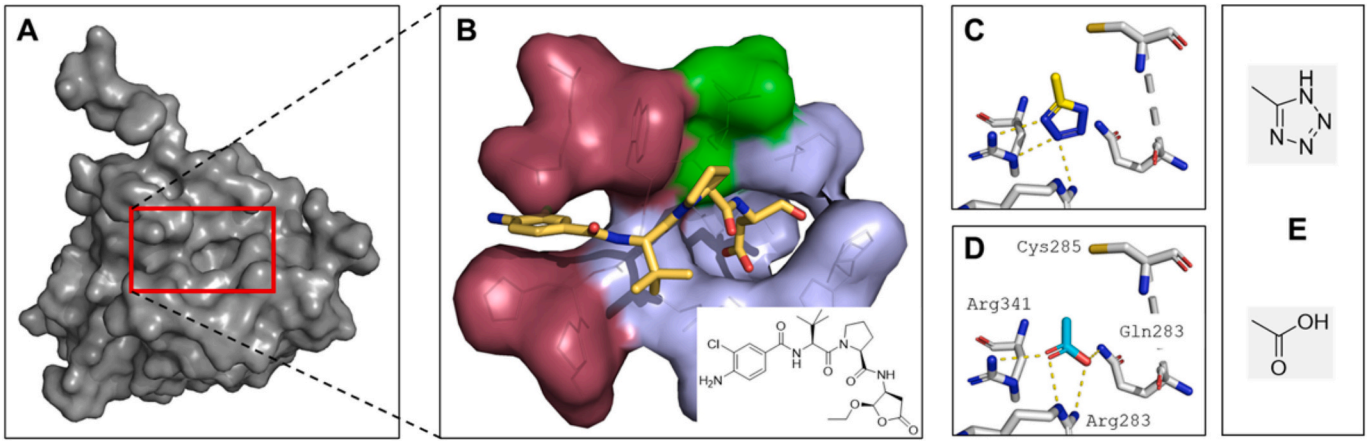

Fig. 3. Design of tetrazole-based non-covalent caspase-1 inhibitors. A) Overall caspase-1 structure surface representation (PDB ID 2HBQ). B) Zoom-into the active site with the covalent Belnacasan (VRT-043198, the agent metabolite of Belnacasan) shown as yellow sticks and the 2D structure insert (PDB ID 6PZP). The three sub binding sites, the active site including the catalytical cysteine, a shallow S2, and a deep groove are marked in blue, green and red colors, respectively. C) Docking of a 5-methyl tetrazolate into the active site and comparison, D) with a carboxylate, with the hydrogen bonds indicated as yellow dotted lines. E) 2D structures of the docked fragments. (For interpretation of the references to colour in this figure legend, the reader is referred to the web version of this article.)

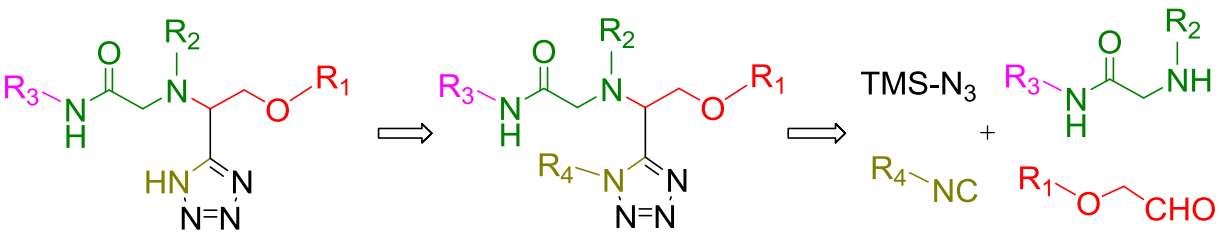

Scheme 1. Retrosynthesis and scaffold-building block relationship

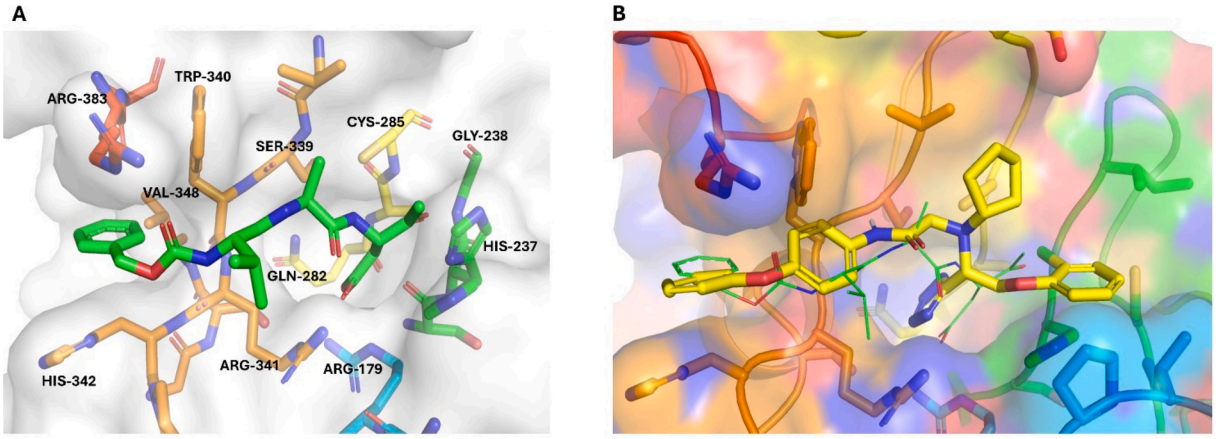

Fig. 4. (A) Key amino acids in the caspase-1 active site (PDB ID: 2HBQ); (B) docked pose of compound ***S*-6e** (yellow sticks) superimposed on the co-crystallized peptide inhibitor z-VAD-FMK (green lines). (For interpretation of the references to colour in this figure legend, the reader is referred to the web version of this article.)

2.3. Biological activity assessment

2.3.1. Caspase-1 inhibition activities

The inhibitory activity of compounds **6a–g** against caspase-1 was evaluated by monitoring the increase in fluorescence over time using the fluorogenic substrate YVAD-AFC. Table 1 summarizes the inhibitory activity of the compounds that showed measurable activity within the concentration range tested, reported as IC_{50} values together with the residual enzymatic activity measured at 100 μM. Compounds **6a** and **6g** were inactive at the highest tested concentration (100 μM) and are therefore not included in Table 1. Modulation of the hydrophobic R_2 substituent markedly influenced inhibitory potency. Among the synthesized derivatives, compounds **6e** and **6f** exhibited the highest activity, with IC_{50} values of 380 and 360 nM, respectively (Fig. 5). Compared with the most active compounds of our previously reported 1,5-disubstituted α-aminotetrazole series (IC_{50} = 10.3–15.1 μM),35 compounds **6e** and **6f** displayed an approximately 30-fold improvement in enzymatic potency, highlighting the benefits of the newly designed 1*H*-tetrazole-based series. Although these compounds showed potent inhibition of caspase-1, their selectivity toward other caspases and related cysteine proteases remains to be established.

2.3.2. Preliminary in Vivo studies of global force and resistance of dystrophic mdx mice treated with caspase-1 inhibitor *6e* and toxycity evaluation on muscle cells

Duchenne muscular dystrophy (DMD) is a severe X-linked neuromuscular disorder caused by mutations in the dystrophin gene, leading to progressive muscle degeneration, chronic inflammation, and loss of ambulation.43 Although therapeutic strategies have traditionally focused on restoring dystrophin expression or limiting muscle damage, increasing evidence highlights a key contribution of inflammatory pathways to disease progression. In particular, the NLRP3 inflammasome–caspase-1 axis has been implicated in sustaining the chronic inflammatory environment observed in DMD.47,48 The NLRP3 inflammasome is a cytosolic multiprotein complex that responds to cellular stress and promotes caspase-1 activation,49 which in turn processes pro-IL-1β and pro-IL-18 into their active cytokine forms, amplifying inflammation and contributing to muscle degeneration and impaired regeneration.50 Pharmacological and genetic inhibition of this pathway has shown beneficial effects in preclinical models, including reduced inflammation and improved muscle function.51 These findings support caspase-1 as a potential therapeutic target in inflammatory components of DMD. In the present preliminary study, muscle strength was evaluated using the grip strength test in healthy and mdx mice treated with compound **6e** over a two-week period (5–7 weeks of age) (Fig. 6), corresponding to the early phase of disease onset and peak inflammation in this model.52 Although based on a limited number of animals, treatment with compound **6e** was associated with a trend toward improved muscle strength compared with untreated mdx controls. Given the exploratory nature of the study and the absence of direct inflammatory or mechanistic readouts, these effects should be interpreted as preliminary functional observations rather than evidence of direct caspase-1 or inflammasome modulation.

Importantly, the toxicity of compound **6e** was also evaluated in muscle cells at different concentrations, and no toxic effects were observed, supporting its potential safety profile (Fig. 7).

2.4. Molecular dynamic study

The non-cleavable aspartyl-mimicking scaffolds were designed to lack reactive electrophilic functionalities expected to promote covalent interaction with the catalytic cysteine. Molecular dynamics simulations of compound **6e** were conducted to assess the stability of the proposed binding mode within the caspase-1 active site and to elucidate the interactions of the tetrazole warhead and substrate-mimicking side chains responsible for molecular recognition (Fig. 8).

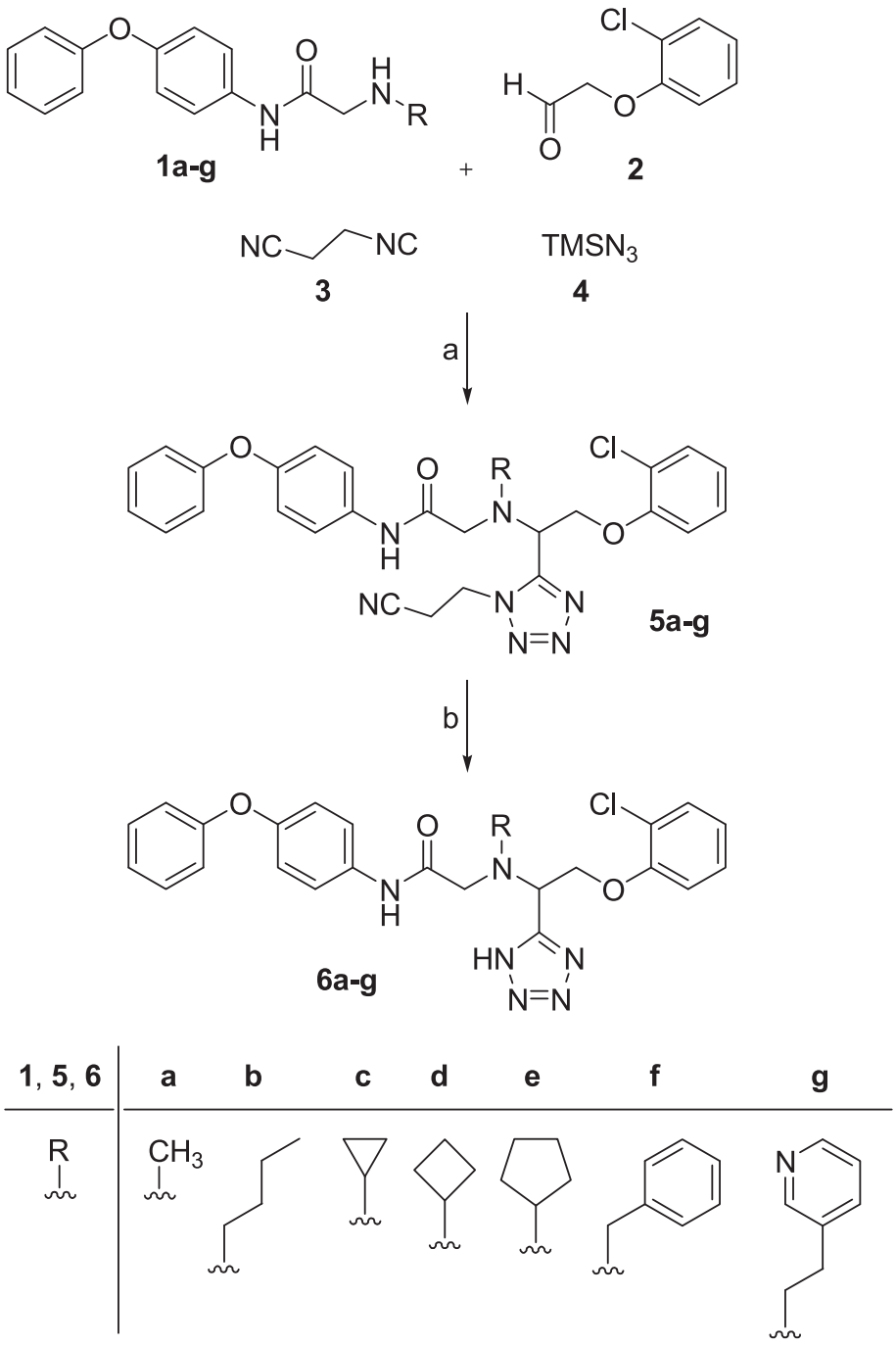

Scheme 2. Synthesis of target compounds **6a-g**. Reagents and conditions: (a) MeOH, r.t., 24-48 h; (b) LiOH, THF:MeOH:H_2O (1:1:1), r.t., 2 h.

Molecular dynamic simulation was performed on the docked poses of the two enantiomer of compound **6e** and on the apo-protein for a total of 200 ns each. The crystal ligand (WEO) from the PDB structure 5MMV was selected as an internal standard due to its carboxylic acid moiety targeting the basic pocket formed by Arg 341 and Arg 179, and its non-covalent nature making it a suitable reference for comparison (Fig. 8). The RMSD (Root Mean Square Deviation) of **6e** and WEO was plotted throughout the trajectory (Fig. 9A).

The molecular dynamics analysis showed, as expected, a significant discrepancy between the binding poses of the two enantiomers of **6e** (Fig. 9A).

The ***R*-6e** enantiomer is less stable in the pocket than the ***S*-6e** enantiomer, likely due to the repositioning of the biphenyl ether, which no longer contacts the S4 sub-pocket but instead interacts with the S1' sub-pocket (Fig. 10). Two-dimensional protein–ligand interaction diagrams for the modeled ***R*-6e** and ***S*-6e** poses are provided in the Supplementary Data (Fig. S1), providing a complementary representation of the predicted interactions.

To complement the visual inspection of the docked poses, static protein–ligand interaction fingerprints were generated with ProLIF[55] for WEO, the previously reported compound 16aa,[35] and the two modeled enantiomers of **6e** (SD, Fig. S2). The ***S*-6e** pose preserved part of the contact network observed for WEO while introducing a prime-side hydrophobic contact with Ile176, consistent with the redesigned P1′–P2′ ligand exit vector.

As for the ***S*-6e** enantiomer, which retains the same configuration as the C1 of WEO (Fig. 8), it is noticeable that the ligand, although less stable than WEO, cycles between two suboptimal stable conformational

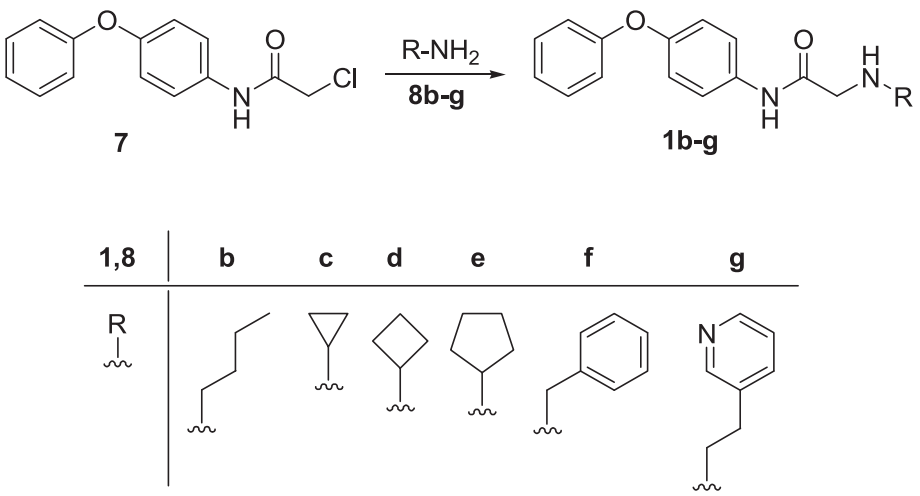

Scheme 3. Synthesis of secondary amines **1b-g**. Reagents and conditions: K_2CO_3, DMF, 60 °C, overnight.

Table 1
In Vitro activities of compounds **6b-f**.[a]

Compound	R_2	IC_{50} (μM)	Enzyme activity (% at 100 μM)
6b	Butyl	0.86	18.59
6c	Cyclopropyl	1.49	9.44
6d	Cyclobutyl	2.36	11.09
6e	Cyclopentyl	0.38	11.70
6f	Benzyl	0.36	13.33
IETD-CHO (standard)		0.06	0

[a] IC_{50} is the concentration of the inhibitor where the enzyme activity is reduced by half.

states while maintaining strong contact with the pocket. It is possible to speculate that such an evident but overall small deviation can be due to a suboptimal initial binding pose.

To evaluate potential conformational changes on the protein side, the RMSF (Root Mean Square Fluctuation) of both WEO, ***R*-6e** and ***S*-6e** was plotted (Fig. 9B). As evident in the chart, no major discrepancies are visible in the general movement of the protein between the two systems.

The observed peaks in fluctuation correspond to the loops that were not modeled but capped. These regions exhibited higher flexibility, which is reflected in the RMSF plot. The similarity in RMSF patterns between the WEO and **6e** systems suggests that the overall protein dynamics are not significantly altered by the binding of **6e** compared to WEO. The latter finding is consistent with the radius of gyration (Fig. 11).

The heatmaps represent the polar contacts between the protein and the ligands (Fig. 12). The carbonyl moiety of the crystal ligand (WEO) demonstrates superior stability in contacting Arg 179 and Arg 341, while the tetrazole struggles to maintain its position due to weaker polar contacts with the arginines (Fig. 12A). Compound ***S*-6e** is stabilized by a different set of interactions that the crystal ligand does not achieve, such as the long-lasting hydrogen bonds with Gly 238 and Cys 285 (Fig. 12B). This additional set of contacts helps the compound stay in the basic pocket, even though it lacks explicit contact with the arginines. Interestingly, compound ***R*-6e**, despite having a "swapped" binding pose (Fig. 10A), seems more capable of interacting with the arginines, although in a suboptimal fashion compared to the crystal ligand. However, when combining this data with the RMSD plot in Fig. 9A, it is likely a coincidence, as the ligand exited the pocket.

Specifically, the interaction bar plots describing protein–ligand contacts were generated and were consistent with the interaction patterns discussed above (Fig. 13). Overall, these simulations suggest that the binding behavior of **6e** may be influenced by stereochemistry, with ***S*-6e** displaying a more persistent interaction pattern than ***R*-6e** under the simulated conditions. Since the biological assays were performed using the unresolved compound **6e**, these findings should be considered a structural hypothesis providing insights into possible binding preferences rather than evidence of stereospecific biological activity. These computational findings also provide preliminary considerations for

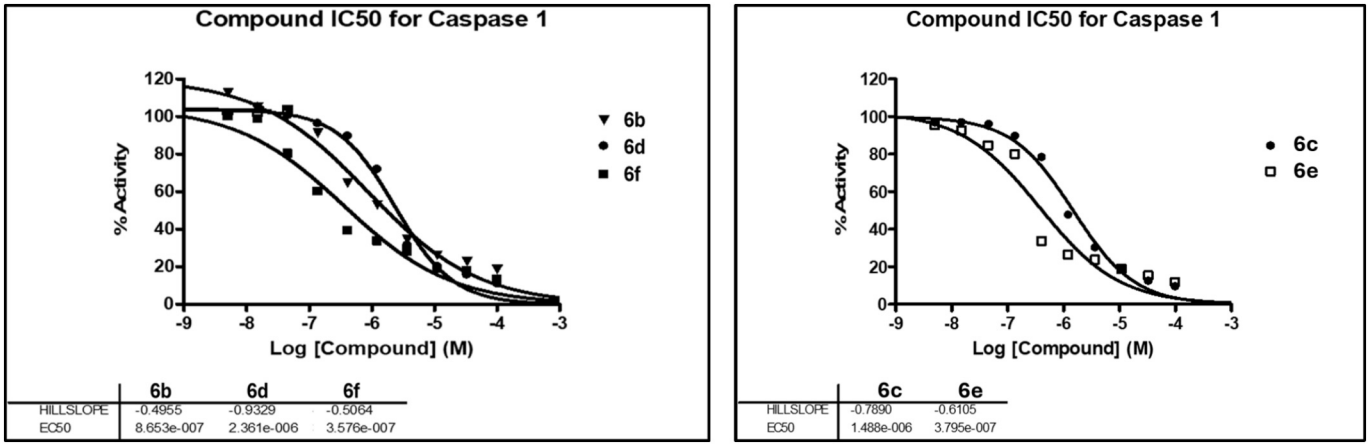

Fig. 5. Inhibition curve of compounds **6b-f**.

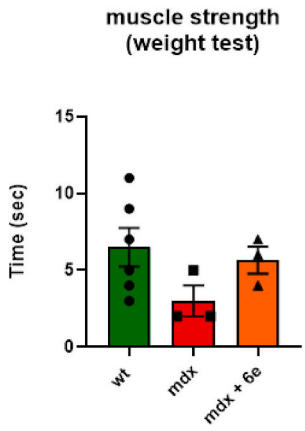

Fig. 6. Effect of compound **6e** on muscle strength (normalized to animal weight) measured in control ($n = 6$) and mdx mice treated with vehicle (DMSO, $n = 3$), **6e** (1 mg Kg^{-1}, $n = 3$).

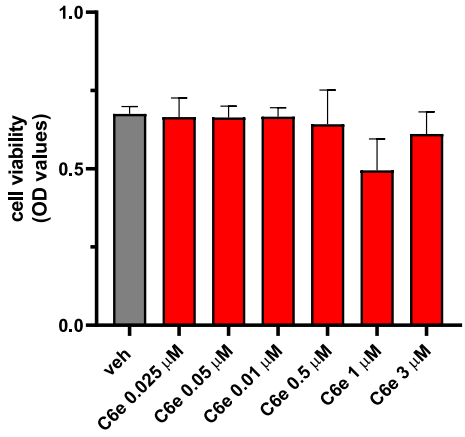

Fig. 7. Cell viability assay (MTT) was assessed using the MTT assay in **C2C12 treated with the indicated concentrations of 6e.** Data are presented as mean ± SEM from four independent experiments.

future optimization of this scaffold. Structure-based approaches integrating molecular docking and computational analysis of ligand–protein interactions can provide useful guidance for the systematic optimization of small-molecule inhibitors.[53,54] In particular, the 1*H*-tetrazole group occupies the S1 region and may serve as an anchoring element, while modifications of the substituents oriented toward the S2–S4 subsites, together with exploration of the S1′–S2′ regions, could be investigated to optimize additional hydrophobic and polar interactions. The different binding behaviors predicted for the two enantiomers of **6e** also suggest that stereochemical optimization may represent a relevant direction for future studies, including the preparation and separate evaluation of the individual enantiomers. Systematic variation of the substituents at these positions, combined with experimental enzymatic and selectivity profiling, may help clarify the contribution of individual structural elements to potency and binding. These considerations are intended as hypotheses for future optimization rather than definitive predictions, and their validity will require experimental investigation.

3. Conclusions

This study describes the design, synthesis, and biological evaluation of a structurally distinct series of 5-substituted 1*H*-tetrazoles as caspase-1 inhibitors. Guided by structure-based drug design and enabled by multicomponent reaction chemistry, this approach led to the identification of potent inhibitors displaying IC_{50} values ranging from the mid-nanomolar to low-micromolar range, with compounds **6e** and **6f** emerging as the most active members of the series (IC_{50} = 380 and 360 nM, respectively). Compared with our previously reported 1,5-disubstituted α-aminotetrazole series, in which the most active compounds displayed caspase-1 inhibitory activity in the low micromolar range (IC_{50} = 10.3–15.1 μM), compounds **6e** and **6f** showed an approximately 30-fold improvement in enzymatic potency. These results support the use of 1*H*-tetrazoles as carboxylic acid bioisosteres for the development of structurally distinct caspase-1 inhibitor scaffolds lacking electrophilic functionalities commonly employed to promote covalent modification of the catalytic cysteine.

Preliminary in vivo evaluation of compound **6e** in a dystrophic mouse model showed a trend toward improved muscle coordination and strength. In parallel, no toxicity was observed in murine muscle cells under the tested conditions. Together, these preliminary findings provide a rationale for further evaluation of this scaffold in expanded preclinical studies. Molecular dynamics simulations suggested distinct binding behaviors, conformational preferences, and interaction patterns for both enantiomers of compound **6e** within the caspase-1 binding pocket, providing insights that may guide future optimization efforts. The contribution of stereochemistry to biological activity, as well as the detailed inhibition mechanism and selectivity profile, remain to be further characterized. Overall, this work identifies a structurally distinct 1*H*-tetrazole-containing scaffold for caspase-1 inhibition and provides a promising starting point for further optimization. Future studies will focus on the generation and evaluation of analogue libraries to further improve potency, the characterization of selectivity against related caspases and cysteine proteases, the investigation of stereochemical effects on biological activity, and the assessment of cellular and pharmacokinetic properties to support further preclinical development.

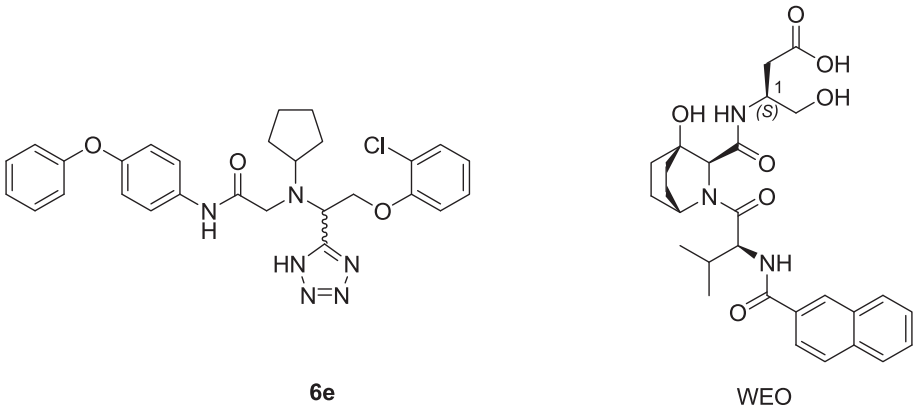

Fig. 8. Ligands objects of Molecular dynamic study.

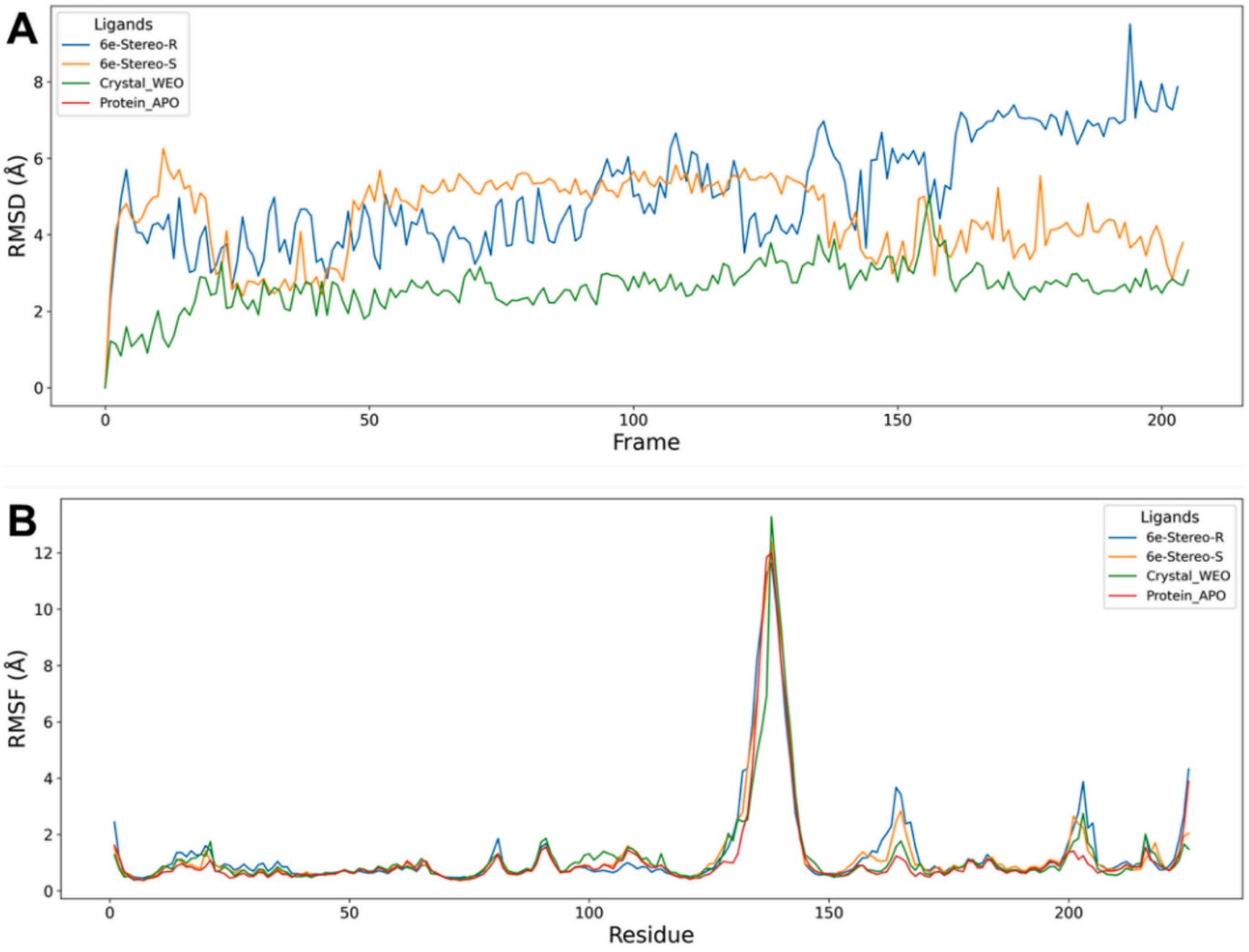

Fig. 9. Geometric analysis of molecular dynamics simulations. (A) RMSD (Root Mean Square Deviation) of the Crystal ligand (WEO, green) and the two enantiomers of compound **6e** (*R*, blue; *S*, orange). The x-axis represents the frame number, while the y-axis shows the RMSD in Ångstroms (Å). (B) RMSF (Root Mean Square Fluctuation) of protein residues when bound to the Crystal ligand WEO, the two enantiomers of **6e** and the apo-protein. The x-axis represents the residue number, while the y-axis shows the RMSF in Ångstroms (Å). (For interpretation of the references to colour in this figure legend, the reader is referred to the web version of this article.)

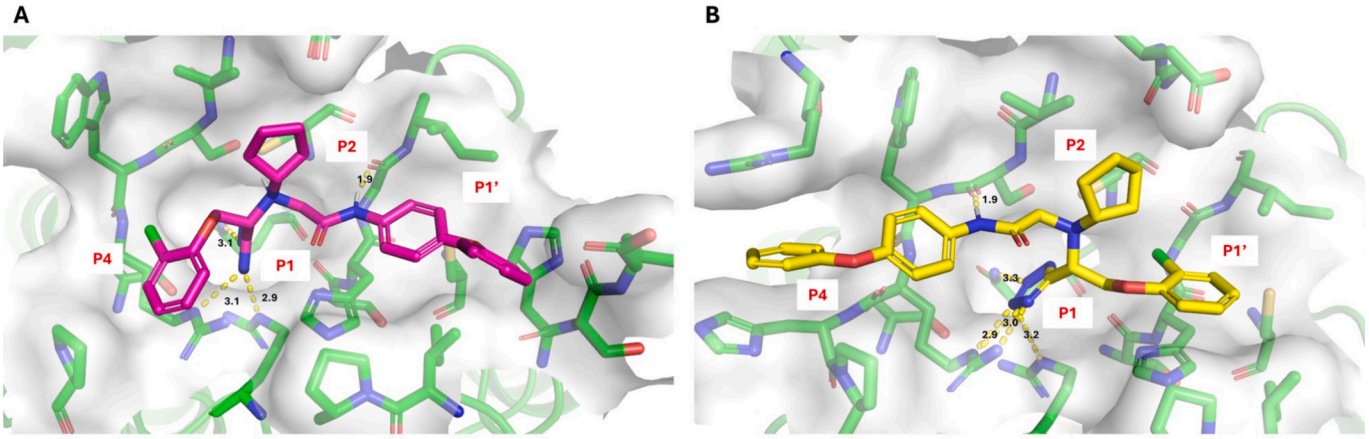

Fig. 10. Docked structures of the tetrazole caspase-1 inhibitor candidate ***R*-6e** (A, magenta) and ***S*-6e** (B, yellow) on 2HBQ receptor. Yellow dashed lines represent modeled *H*-bonds. (For interpretation of the references to colour in this figure legend, the reader is referred to the web version of this article.)

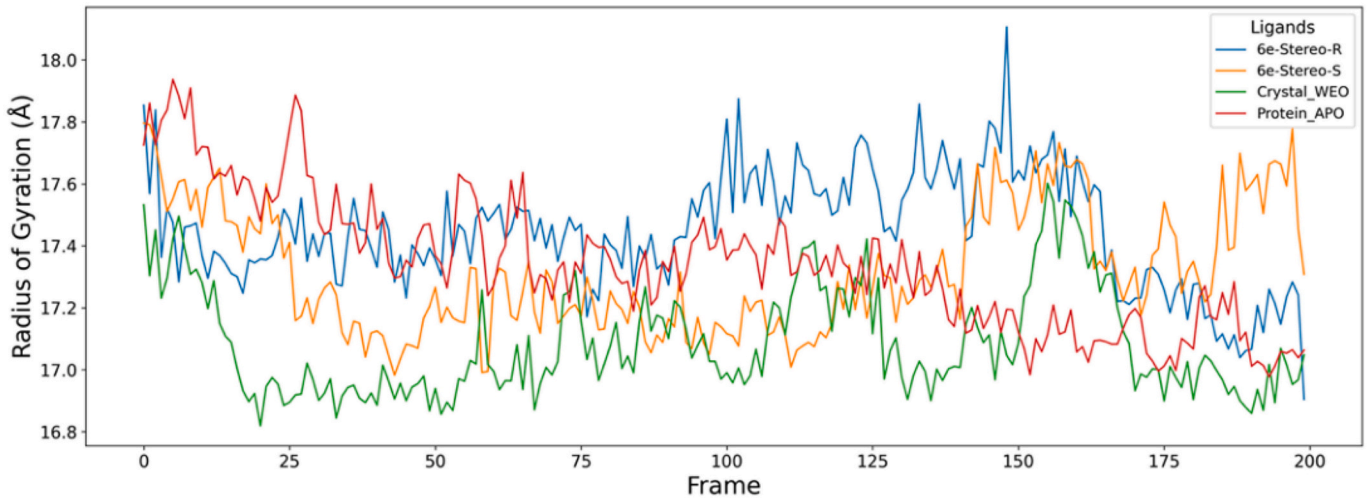

Fig. 11. Radius of Gyration. The structures were superposed based on the alpha carbon atoms, and the radius of gyration was calculated from the mass-weighted positions of the protein's atoms to quantify the compactness of the structures throughout the simulation.

4. Materials and methods

4.1. Computational aided drug discovery

4.1.1. Docking

For our modelling experiments the freeware molecular design software suite MOLOC (http://www.moloc.ch/) was used.56 The standard parameter setting of the software was used as provided by Paul Gerber. The tetrazole molecule was drawn in 2D and converted into 3D coordiantes (Chem 3D) and saved as a sdf file. The receptor (PDB ID 2HBQ) and the tetrazole molecule were imported into Moloc and the small molecule was modeled into the binding site and energy optimized subsequently. Fully flexible docking experiment was conducted on compounds **6e** with the GNINA docking engine. Residue interactions and docking scores are reported to all compounds and the ligand WEO (PDB structure 5MMV) selected as an internal standard due to its carboxylic acid moiety targeting the basic pocket formed by Arg 341 and Arg 179, and its non-covalent nature (Supplementary data). Before interaction analysis, the prepared protein–ligand complexes of both **6e** enantiomers were energy-minimized in situ using MOLOC.

4.1.2. Molecular dynamics

Molecular dynamics simulation was conducted on the docked pose of the analyzed ligands, starting from the protein structure (PDB ID 2HBQ). The missing residues present in the alpha helix between residues 136 and 151 were modeled using AlphaFold, with an in-house developed Python script that extracts the coordinates from the AlphaFold prediction and aligns them to the crystal structure. The missing structure connecting residues 125 and 317 was not modeled and terminal residues capped.

The protein-small molecule complex was solvated into a cubic box with 0.5 nm padding, and the system was neutralized with a physiological concentration (0.15 M) of sodium and chloride ions. Periodic boundary conditions were applied throughout the simulation. The system was prepared using an in-house developed Python script based on the molecular dynamics engine OpenMM with the AMBER ff14SB forcefield for the protein and the OpenFF 2.1.1 forcefield for the ligand.

The system was first minimized using the steepest descent algorithm. This was followed by NVT equilibration for 400 ps using a Langevin integrator, with temperature gradually increased to the target temperature. During NVT, positional restraints were applied to non-water molecules. NPT equilibration was then performed for an additional 400 ns using a Monte Carlo barostat set to 1 bar pressure. Backbone atoms and ligand were restrained, with restraint forces gradually decreased.

Finally, production molecular dynamics was run without restraints for 200 ns. The simulation used a Langevin integrator with a 2 fs timestep. Throughout the simulation, all bonds involving hydrogen atoms were constrained using the HBonds algorithm. Particle Mesh Ewald was used for long-range electrostatics. The center of mass motion was not removed, as specified in the forcefield parameters. The hydrogen mass was repartitioned to 2 amu to allow for a larger time step. The trajectories were centered, and periodic boundary conditions (PBC) were removed to perform the analysis described above. The geometric analysis was conducted using PyTraj and MDAnalysis, while the interactions were computed with ProLIF.55

4.2. Chemistry

All reagents were chemically pure or analytically pure products and were not further purified. The ^{1}H NMR and ^{13}C NMR spectra were measured on a Bruker BioSpin GmbH spectrometer (Bruker Company, Karlsruhe, Germany) at 400 and 100 MHz, respectively. $CDCl_3$ was used as solvent. TMS was used as the internal standard, the chemical shift unit was ppm, and the coupling constant unit was Hz. Proton coupling modes were described as singlet (s), broad singlet (brs), doublet (d), doublet of doublets (dd), triplet (t), and multiplet (m). Mass spectra were measured on a Waters Investigator Supercritical Fluid Chromatograph with a 3100 MS Detector (ESI) (SFC-MS) using a solvent system of methanol and CO_2 on a Viridis silica gel column (4.6 × 250 mm, 5 μm particle size) and reported as (*m/z*). Elemental analyses were performed with a Thermo Scientific Flash*Smart* CHN analyzer, and results were within 0.4% of the calculated values. All final compounds were characterized by elemental analysis, ^{1}H NMR spectroscopy, and LC–MS. Elemental analysis values were consistent with the proposed molecular formulae, the ^{1}H NMR spectra showed no significant detectable impurities, and LC–MS analysis confirmed the expected molecular ions together with a single predominant chromatographic peak.

4.3. Synthetic procedures

4.3.1. General procedure for the preparation of compounds *6a-g*

To a solution of suitable secondary amine **1a-g** (1 mmol) in MeOH (1 mL), aldehyde **2** (1 mmol), isocyanide **3** (1 mmol) and trimethylsilylazide **4** (1 mmol) were added. The reaction mixture was stirred at room temperature for 24-48 h. The solvent was removed under reduced pressure followed by purification by flash chromatography on silica gel eluting with hexane/ethyl acetate to afford desired products **5a-g**.

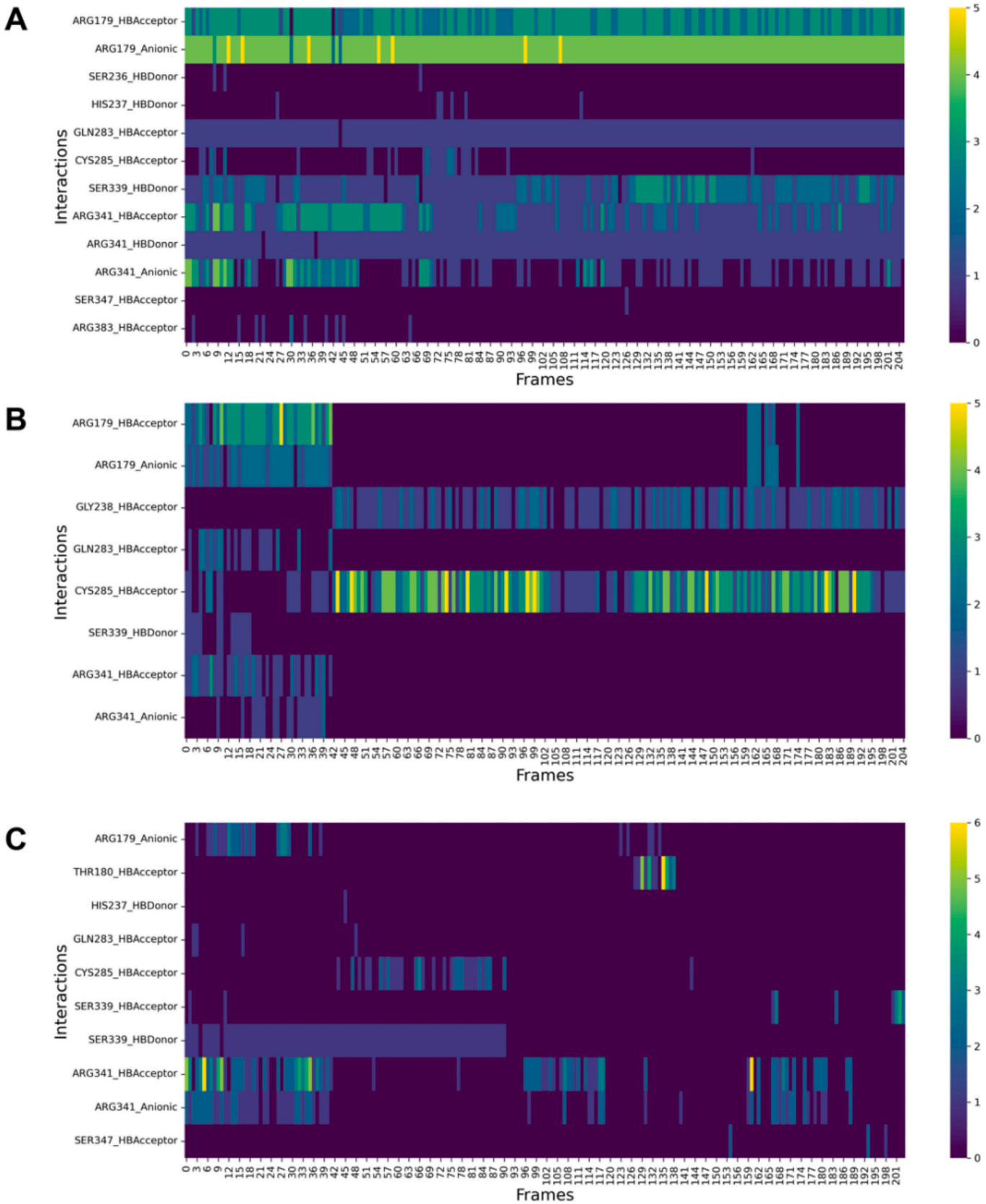

Fig. 12. Polar contacts analysis along the trajectories of Crystal WEO (A), compound ***S*-6e** (B), and compound ***R*-6e**, (C) shows the distribution of contacts over time. On the x-axis, the frames of the trajectory are represented, while the y-axis indicates the types of polar contacts. In the heatmap, the colour gradient from blue to yellow represents the increasing number of relative contacts. (For interpretation of the references to colour in this figure legend, the reader is referred to the web version of this article.)

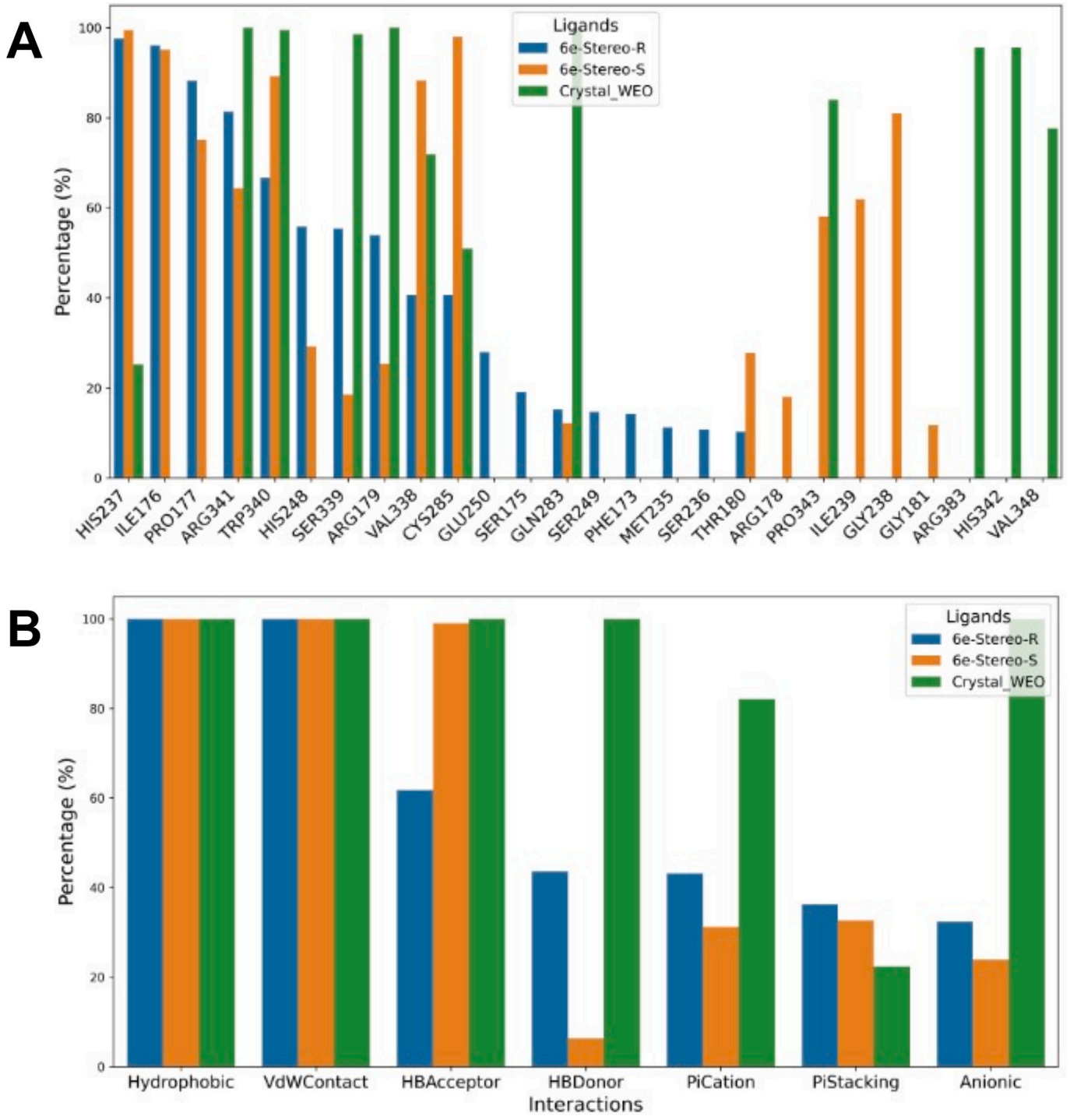

Fig. 13. Percentage of interactions of different ligands throughout the entire trajectory: (A) residue-grouped bar plot; (B) interaction-grouped bar plot.

To a solution of appropriate compound **5a-g** (0.2 mmol) in 4 mL of THF:MeOH:H_2O (1:1:1) cooled to 0 °C, LiOH (17 mg, 0.4 mmol) was added. The reaction mixture was allowed to stir at room temperature for 2 h. Then, the solvent was removed under reduced pressure, the residue was dissolved in water and cooled in ice. Addition of 1 N HCl gave a precipitated product. The solvent was removed under reduced pressure and the residue was purified by flash column chromatography on silica gel eluting with methanol/DCM to afford target products **6a-g**.

4.3.2. Characterization details

2-((2-(2-Chlorophenoxy)-1-(1*H*-tetrazol-5-yl)ethyl)(methyl)amino)-*N*-(4-phenoxyphenyl)acetamide **6a**.

White solid. Mp: 114–116 °C. Yield: 26% (from **1a**). ^{1}H NMR (400 MHz, $CDCl_3$) δ 9.42 (s, 1H), 7.51 (d, J = 8.9, 2H), 7.37 (dd, J = 7.9, 1.4, 1H), 7.35–7.29 (m, 2H), 7.25–7.19 (m, 1H), 7.09 (t, J = 7.4, 1H), 7.05 (d, J = 8.2, 1H), 7.01–6.92 (m, 5H), 4.76 (dd, J = 9.4, 4.3, 1H), 4.65 (t, J = 9.9, 1H), 4.52 (dd, J = 10.3, 4.3, 1H), 3.71–3.53 (m, 2H), 2.54 (s, 3H). ^{13}C NMR (100 MHz, $CDCl_3$) δ 170.5, 157.2, 154.4, 153.5, 132.0, 130.5, 129.8, 128.2, 123.3, 122.9, 122.6, 119.4, 118.7, 114.4, 67.1, 58.4, 58.0, 39.1 ppm. MS (ESI) m/z calculated $[M + H]^+$: 479.13; found $[M + H]^+$: 479.26. Anal. Calcd for $C_{24}H_{23}ClN_6O_3$: C, 60.19; H, 4.84; N, 17.55. Found: C, 60.04; H, 4.83; N, 17.52.

2-(Butyl(2-(2-chlorophenoxy)-1-(1*H*-tetrazol-5-yl)ethyl)amino)-*N*-(4-phenoxyphenyl)acetamide **6b**.

White solid. Mp: 112–115 °C. Yield: 35% (from **1b**). ^{1}H NMR (400 MHz, $CDCl_3$) δ 9.75 (s, 1H), 7.46 (d, J = 8.9, 2H), 7.36–7.28 (m, 3H), 7.19 (t, J = 7.2, 1H), 7.08 (t, J = 7.4, 1H), 7.00 (d, J = 8.0, 1H), 6.97–6.88 (m, 5H), 4.87 (dd, J = 9.9, 3.9, 1H), 4.64 (t, J = 10.2, 1H), 4.43 (dd, J = 10.4, 4.0, 1H), 3.74 (d, J = 17.8, 1H), 3.44 (d, J = 17.8, 1H), 2.91–2.79 (m, 1H), 2.75–2.57 (m, 1H), 1.69–1.49 (m, 2H), 1.49–1.38 (m, 1H), 1.38–1.29 (m, 1H), 0.88 (t, J = 7.3, 3H). ^{13}C NMR (100 MHz, $CDCl_3$) δ 171.5, 157.2, 156.6, 154.3, 153.5, 132.1, 130.5, 129.8, 128.1, 123.3, 122.9, 122.7, 122.7, 119.4, 118.6, 114.2, 67.2, 56.4, 55.5, 52.8, 30.4, 20.2, 13.9 ppm. MS (ESI) *m/z* calculated $[M + H]^+$: 521.20; found $[M + H]^+$: 521.41. Anal. Calcd for $C_{27}H_{29}ClN_6O_3$: C, 62.24; H, 5.61; N, 16.13. Found: C, 62.08; H, 5.59; N, 16.09.

2-((2-(2-Chlorophenoxy)-1-(1*H*-tetrazol-5-yl)ethyl)(cyclopropyl)amino)-*N*-(4-phenoxyphenyl)acetamide **6c**.

Yellow solid. Mp: 122–124 °C. Yield: 36% (from **1c**). ^{1}H NMR (400 MHz, $CDCl_3$) δ 9.48 (s, 1H), 7.42–7.37 (m, 2H), 7.32–7.27 (m, 3H), 7.17 (td, J = 8.3, 1.5, 1H), 7.07 (t, J = 7.4, 1H), 6.98 (d, J = 8.3, 1H), 6.92 (d, J = 8.3, 2H), 6.90–6.84 (m, 3H), 4.91 (dd, J = 10.2, 4.0, 1H), 4.71 (t, J = 10.2, 1H), 4.49 (dd, J = 10.2, 4.0, 1H), 3.83 (d, J = 17.7, 1H), 3.68 (d, J = 17.6, 1H), 2.50–2.36 (m, 1H), 0.78–0.68 (m, 1H), 0.66–0.50 (m, 3H). ^{13}C NMR (100 MHz, $CDCl_3$) δ 172.1, 157.2, 154.5, 153.3, 131.8, 130.1, 129.8, 128.2, 123.3, 123.1, 122.6, 122.5, 119.3, 118.6, 113.7, 66.6, 57.6, 56.5, 35.4, 7.9, 6.6 ppm. MS (ESI) *m/z* calculated $[M + H]^+$: 505.17; found $[M + H]^+$: 505.32. Anal. Calcd for $C_{26}H_{25}ClN_6O_3$: C, 61.84; H, 4.99; N, 16.64. Found: C, 61.71; H, 4.97; N, 16.61.

2-((2-(2-Chlorophenoxy)-1-(1*H*-tetrazol-5-yl)ethyl)(cyclobutyl)amino)-*N*-(4-phenoxyphenyl)acetamide **6d**.

White solid. Mp: 140–143 °C. Yield: 32% (from **1d**). ^{1}H NMR (400 MHz, $CDCl_3$) δ 9.69 (s, 1H), 7.45 (d, J = 8.9, 2H), 7.38–7.28 (m, 4H), 7.17 (t, J = 7.1, 1H), 7.08 (t, J = 7.4, 1H), 6.98–6.91 (m, 4H), 6.90 (d, J = 8.8, 2H), 4.81 (dd, J = 9.8, 4.0, 1H), 4.55 (t, J = 10.1, 1H), 4.42 (dd, J = 10.3, 4.1, 1H), 3.69 (d, J = 17.9, 1H), 3.65–3.55 (m, 1H), 3.42 (d, J = 17.8, 1H), 2.14–1.90 (m, 4H), 1.77–1.65 (m, 1H), 1.64–1.52 (m, 1H). ^{13}C NMR (100 MHz, $CDCl_3$) δ 172.0, 157.3, 154.1, 153.4, 132.2, 130.5, 129.7, 128.1, 123.2, 122.9, 122.6, 122.4, 119.4, 118.5, 114.0, 67.2, 56.5, 54.9, 51.4, 28.5, 28.2, 14.4 ppm. MS (ESI) *m/z* calculated $[M + H]^+$: 519.18; found $[M + H]^+$: 519.42. Anal. Calcd for $C_{27}H_{27}ClN_6O_3$: C, 62.48; H, 5.24; N, 16.19. Found: C, 62.36; H, 5.23; N, 16.17.

2-((2-(2-Chlorophenoxy)-1-(1*H*-tetrazol-5-yl)ethyl)(cyclopentyl)amino)-*N*-(4-phenoxyphenyl)acetamide **6e**.

Yellow solid. Mp: 195–196 °C. Yield: 30% (from **1e**). ^{1}H NMR (400 MHz, $CDCl_3$) δ 9.76 (s, 1H), 7.47 (d, J = 8.9, 2H), 7.37 (dd, J = 7.9, 1.5, 1H), 7.36–7.31 (m, 2H), 7.25–7.20 (m, 1H), 7.11 (t, J = 7.4, 1H), 7.05–7.00 (m, 1H), 6.99–6.96 (m, 3H), 6.94 (d, J = 8.9, 2H), 5.01 (dd, J = 9.5, 3.6, 1H), 4.62 (t, J = 10.1, 1H), 4.47 (dd, J = 10.4, 4.1, 1H), 3.81 (d, J = 18.2, 1H), 3.53 (d, J = 18.1, 1H), 3.49–3.37 (m, 1H), 2.01–1.82 (m, 2H), 1.79–1.65 (m, 2H), 1.64–1.39 (m, 4H). ^{13}C NMR (100 MHz, $CDCl_3$) δ 172.6, 157.3, 154.2, 153.4, 132.0, 130.5, 129.8, 128.2, 123.2, 122.7, 122.5, 119.4, 118.6, 114.2, 67.5, 56.4, 53.4, 52.4, 30.8, 30.7, 23.6, 23.5 ppm. MS (ESI) *m/z* calculated $[M + H]^+$: 533.20; found $[M + H]^+$: 533.33. Anal. Calcd for $C_{28}H_{29}ClN_6O_3$: C, 63.09; H, 5.48; N, 15.77. Found: C, 62.93; H, 5.46; N, 15.74.

2-(Benzyl(2-(2-chlorophenoxy)-1-(1*H*-tetrazol-5-yl)ethyl)amino)-*N*-(4-phenoxyphenyl)acetamide **6f**.

White solid. Mp: 99–101 °C. Yield: 45% (from **1f**). ^{1}H NMR (400 MHz, $CDCl_3$) δ 9.55 (s, 1H), 7.45 (d, J = 7.3, 2H), 7.37–7.32 (m, 4H), 7.31–7.28 (m, 3H), 7.26–7.22 (m, 1H), 7.21–7.15 (m, 1H), 7.09 (t, J = 7.4, 1H), 7.00–6.96 (m, 1H), 6.95 6.92 (m, 3H), 6.91–6.88 (m, 2H), 4.89 (dd, J = 10.2, 4.1, 1H), 4.70 (t, J = 10.4, 1H), 4.45 (dd, J = 10.5, 4.1, 1H), 4.10 (d, J = 13.3, 1H), 3.78–3.63 (m, 2H), 3.47 (d, J = 17.5, 1H). ^{13}C NMR (100 MHz, $CDCl_3$) δ 171.2, 157.2, 154.3, 153.4, 138.9, 131.8, 130.5, 129.8, 128.7, 128.6, 128.1, 126.5, 123.3, 122.8, 119.3, 118.6, 114.3, 67.5, 56.5, 55.5, 34.7 ppm. MS (ESI) *m/z* calculated $[M + H]^+$: 555.18; found $[M + H]^+$: 555.34. Anal. Calcd for $C_{30}H_{27}ClN_6O_3$: C, 64.92; H, 4.90; N, 15.14. Found: C, 64.81; H, 4.89; N, 15.12.

2-((2-(2-Chlorophenoxy)-1-(1*H*-tetrazol-5-yl)ethyl)(2-(pyridin-3-yl)ethyl)-amino)-*N*-(4-phenoxyphenyl)acetamide **6g**.

Yellow solid. Yield: 26% (from **1g**). ^{1}H NMR (400 MHz, $CDCl_3$) δ 9.29 (s, 1H), 8.67 (d, J = 4.6, 1H), 7.71 (t, J = 7.4, 1H), 7.35–7.25 (m, 5H), 7.23–7.13 (m, 3H), 7.06 (t, J = 7.4, 1H), 6.96 (d, J = 8.1, 1H), 6.93–6.87 (m, 3H), 6.82 (d, J = 8.8, 2H), 4.92 (d, J = 6.2, 1H), 4.63 (dd, J = 10.0, 3.1, 1H), 4.53 (t, J = 9.9, 1H), 3.93 (d, J = 17.7, 1H), 3.69 (d, J = 17.6, 1H), 3.40 (t, J = 5.3, 2H), 3.31–3.10 (m, 2H). ^{13}C NMR (100 MHz, $CDCl_3$) δ 169.9, 158.1, 157.5, 156.0, 153.5, 153.4, 146.4, 139.5, 132.7, 130.4, 129.7, 128.1, 125.3, 123.1, 122.8, 122.6, 122.4, 121.6, 119.3, 118.4, 113.5, 67.3, 58.3, 57.7, 34.4 ppm. MS (ESI) *m/z* calculated $[M + H]^+$: 570.19; found $[M + H]^+$: 570.35. Anal. Calcd for $C_{30}H_{28}ClN_7O_3$: C, 63.21; H, 4.95; N, 17.20. Found: C, 63.09; H, 4.94; N, 17.17.

4.4. Biological evaluation

4.4.1. Caspase-1 inhibition (provided by reaction biology CRO)

The caspase-1 assay protocol is based on the cleavage of substrate YVAD-AFC (AFC: 7-amino-4-trifluoromethyl coumarin). YVAD-AFC emits blue light (Em = 400 nm); upon cleavage of the substrate by caspase-1, free AFC emits a yellow-green fluorescence (Ex/Em = 400/505 nm). Comparison of the fluorescence from a treated sample with an untreated control allows determination of the fold increase in caspase-1 activity. Compounds exhibit no fluorescent background that could interfere with the assay. All synthesized compounds were tested 10-dose IC_{50} with 3-fold serial dilution starting at 100 μM or 10 μM against caspase-1. Control compounds were tested in a 10-dose IC_{50} with 3-fold serial dilution starting at 10 μM.

4.4.2. Cell viability assay

Cell viability was measured using the 3-(4,5-Dimethylthiazol-2-yl)-2,5-diphenyltetrazolium bromide (MTT) assay. In brief, C2C12 cells were seeded in 24-well culture plates (25,000 cells/well) and allowed to attach overnight before starting the treatment with C6e for an additional 24 h. After this time, cell media was replaced by MTT solution (0.5 mg/mL, pH 7.4) for 3 h at 37 °C. Formazan precipitates formed were dissolved using an isopropanol solution, and absorbance was recorded at 595 nm using a Promega GloMax Plate Reader according to published procedures.[57]

4.4.3. Cell culture and reagents

Murine C2C12 myoblasts were propagated in a growth medium (GM) composed of Dulbecco's modified Eagle's medium (cat# 11995065; Life Technologies) supplemented with 10% fetal bovine serum (FBS, cat# 16000044; Life Technologies), 5000 U/mL penicillin plus 5000 μg/mL streptomycin (cat# 15070063; Life Technologies), and 1% L-glutamine (cat# A2916801; Life Technologies). C2C12 cells were routinely tested for mycoplasma contamination using the PCR Mycoplasma Test Kit (cat# MP0050).

4.4.4. Animal model and drug treatment

The Animal Study Protocol (IACUC; 536/2018) was approved by the Italian Ministry of Health and Ethics Committee for the use of experimental animals being conformed to guidelines for the safe use and care of experimental animals following the Italian D.L. no. 116 of 27 January 1992 and associated guidelines in the European Communities Council (86/609/ECC and 2010/63/UE). In this study, male 5 weeks old control (C57BL/10ScSnJ) and dystrophic (C57BL/10ScSn-DMDmdx/J) mice weighing approximately 20–25 g were purchased from Charles River Laboratories (Milan IT). All mice were housed in an individually ventilated cage system with a 12-h light-dark cycle and received standard mouse chow (Harlan Teklad) and water *ab libitum*. Animals belonging to each cage were randomly assigned to the different experimental groups. The experimenter(s) performing the treatments and locomotor testing was blind to the genotype and treatment. Compound

6e (1 $mgKg^{-1}$). was intraperitoneally (IP) injected three times a week for 2 weeks according to published procedures.52

4.4.5. Treatment and locomotor tests

Control (C57BL/10ScSnJ) or dystrophic (C57BL/10ScSn-DMDmdx/J) mice were intraperitoneally (IP) injected with **6e** (1 $mgKg^{-1}$) three times per week for 2 weeks. To test the forelimb strength of dystrophic mice treated or not with **6e**, four weights of 20, 33, 46, and 59 g were used. Mice were handled by the base of the tail and were allowed to grip the first weight (20 g) and a hold of 3 s was the criterion. If the mouse dropped the weight in less than 3 s, we tried the same weight again for a maximum of three times. If the mouse held it for 3 s, then we tried it on the next heaviest weight. The mouse was assigned the maximum time/weight achieved. The final total score is calculated as the product of the number of links in the heaviest chain held for the full 3 s multiplied by the time (s) it is held.

CRediT authorship contribution statement

Ajay L. Chandgude: Investigation, Formal analysis, Data curation. **Giovanni Loriga:** Writing – review & editing, Data curation. **Andrea Beccu:** Formal analysis, Data curation. **Fabio Arturo Iannotti:** Writing – review & editing, Validation, Investigation. **Ester Pagano:** Validation, Investigation. **Raffaele Capasso:** Validation, Investigation. **Riccardo Fusco:** Software, Investigation, Formal analysis, Data curation. **Pietro Spanu:** Writing – review & editing, Writing – original draft, Supervision, Methodology, Funding acquisition, Conceptualization. **Fausta Ulgheri:** Writing – review & editing, Supervision, Methodology, Funding acquisition, Conceptualization. **Alexander Domling:** Writing – review & editing, Supervision, Methodology, Funding acquisition, Conceptualization.

Funding

This research was funded by Regione Sardegna, grant number CRP 59740, and Progetto Omnibus legge Regionale n.7. Italian Ministry of University and Research, grant number PRIN 2020 – AEX4TA.

Declaration of competing interest

The authors declare the following financial interests/personal relationships which may be considered as potential competing interests: Alexander Domling, Pietro Spanu, and Fausta Ulgheri are co-inventors of patent application EP3666769A1 (“Novel Caspase Inhibitors”), which included compounds related to the present study. The patent application was subsequently withdrawn and is not currently in force. The authors declare that they have no other competing financial interests or personal relationships that could have influenced the work reported in this paper.

Acknowledgements

We acknowledge IT4Innovation, Czech Republic for awarding this project access to the LUMI supercomputer, owned by the EuroHPC Joint Undertaking, hosted by CSC (Finland) and the LUMI consortium through IT4Innovation, Czech Republic. This research was funded by the ERA Chair grant ACCELERATOR (101087318) and the ERC Advanced grant AMADEUS (101098001) and the VIDEC grant (872195). This study was supported (to AD) the project National Institute for Cancer Research (Programme EXCELES, ID Project No. LX22NPO5102) - Funded by the European Union – Next Generation EU and the Dutch Cancer Society (KWF Kankerbestrijding, KWF) grant (14712).

Ethics declaration

Animal subject

This study was conducted in accordance with the following guidelines for animal welfare and/or reporting: Italian D.L. no. 116 of 27 January 1992 and associated guidelines in the European Communities Council (86/609/ECC and 2010/63/UE).

This study was approved by the Italian Ministry of Health and Ethics Committee.

(Approval No. Approval No. IACUC; 536/2018)

Appendix A. Supplementary data

Supplementary data to this article can be found online at https://doi.org/10.1016/j.bmc.2026.118794.

Data availability

Data will be made available on request.

References

1. Zheng D, Liwinski T, Elinav E. Inflammasome activation and regulation: toward a better understanding of complex mechanisms. *Cell Discov*. 2020;6:36. https://doi.org/10.1038/s41421-020-0167-x.
2. Chauhan D, Vande Walle L, Lamkanfi M. Therapeutic modulation of inflammasome pathways. *Immunol Rev*. 2020;297(1):123–138. https://doi.org/10.1111/imr.12908.
3. Samir P, Malireddi RKS, Kanneganti TD. The PANoptosome: A deadly protein complex driving Pyroptosis, apoptosis, and necroptosis (PANoptosis). *Front Cell Infect Microbiol*. 2020;10:238. https://doi.org/10.3389/fcimb.2020.00238.
4. Chen W, Gullett JM, Tweedell RE, Kanneganti TD. Innate immune inflammatory cell death: PANoptosis and PANoptosomes in host defense and disease. *Eur J Immunol*. 2023;53(11), e2250235. https://doi.org/10.1002/eji.202250235.
5. Piancone F, La Rosa F, Marventano I, Saresella M, Clerici M. The role of the inflammasome in neurodegenerative diseases. *Molecules*. 2021;26(4):953. https://doi.org/10.3390/molecules26040953.
6. Blevins HM, Xu Y, Biby S, Zhang S. The NLRP3 Inflammasome pathway: A review of mechanisms and inhibitors for the treatment of inflammatory diseases. *Front Aging Neurosci*. 2022;14, 879021. https://doi.org/10.3389/fnagi.2022.879021.
7. Wang L, Zhu Y, Zhang L, et al. Mechanisms of PANoptosis and relevant small-molecule compounds for fighting diseases. *Cell Death Dis*. 2023;14(12):851. https://doi.org/10.1038/s41419-023-06370-2.
8. Molla MD, Akalu Y, Geto Z, Dagnew B, Ayelign B, Shibabaw T. Role of caspase-1 in the pathogenesis of inflammatory-associated chronic noncommunicable diseases. *J Inflamm Res*. 2020;13:749–764. https://doi.org/10.2147/JIR.S277457.
9. Chen X, Deng G, Chen K, Chen Y, Ye W, Sun P. Targeting the NLRP3 inflammasome in psoriasis. *Int J Dermatol*. 2024;63(7):844–851. https://doi.org/10.1111/ijd.17073.
10. Molla MD, Ayelign B, Dessie G, Geto Z, Admasu TD. Caspase-1 as a regulatory molecule of lipid metabolism. *Lipids Health Dis*. 2020;19(1):34. https://doi.org/10.1186/s12944-020-01220-y.
11. Wang T, Ruan B, Wang J, et al. Activation of NLRP3-Caspase-1 pathway contributes to age-related impairments in cognitive function and synaptic plasticity. *Neurochem Int*. 2022;152, 105220. https://doi.org/10.1016/j.neuint.2021.105220.
12. Lin TY, Tsai MC, Tu W, et al. Role of the NLRP3 Inflammasome: insights into Cancer hallmarks. *Front Immunol*. 2021;11, 610492. https://doi.org/10.3389/fimmu.2020.610492.
13. Toldo S, Mezzaroma E, Buckley LF, et al. Targeting the NLRP3 inflammasome in cardiovascular diseases. *Pharmacol Ther*. 2022;236, 108053. https://doi.org/10.1016/j.pharmthera.2021.108053.
14. Flores J, Noël A, Fillion ML, LeBlanc AC. Therapeutic potential of Nlrp1 inflammasome, Caspase-1, or Caspase-6 against Alzheimer disease cognitive impairment. *Cell Death Differ*. 2022;29(3):657–669. https://doi.org/10.1038/s41418-021-00881-1.
15. Sharma B, Satija G, Madan A, et al. Role of NLRP3 Inflammasome and its inhibitors as emerging therapeutic drug candidate for Alzheimer's disease: a review of mechanism of activation, regulation, and inhibition. *Inflammation*. 2023;46(1):56–87. https://doi.org/10.1007/s10753-022-01730-0.
16. Flores J, Noël A, Foveau B, Lynham J, Lecrux C, LeBlanc AC. Caspase-1 inhibition alleviates cognitive impairment and neuropathology in an Alzheimer's disease mouse model. *Nat Commun*. 2018;9(1):3916. https://doi.org/10.1038/s41467-018-06449-x.
17. Wang W, Nguyen LT, Burlak C, et al. Caspase-1 causes truncation and aggregation of the Parkinson's disease-associated protein α-Synuclein. *Proc Natl Acad Sci USA*. 2016;113(34):9587–9592. https://doi.org/10.1073/pnas.1610099113.

18. Ozaki E, Campbell M, Doyle SL. Targeting the NLRP3 inflammasome in chronic inflammatory diseases: current perspectives. *J Inflamm Res*. 2015;8:15–27. https://doi.org/10.2147/JIR.S51250.
19. Liu Z, Wang C, Lin C. Pyroptosis as a double-edged sword: the pathogenic and therapeutic roles in inflammatory diseases and cancers. *Life Sci*. 2023;318, 121498. https://doi.org/10.1016/j.lfs.2023.121498.
20. Gao J, Zhang H, Yang Y, Tao J. Therapeutic potential of targeting the NLRP3 Inflammasome in rheumatoid arthritis. *Inflammation*. 2023;46(3):835–852. https://doi.org/10.1007/s10753-023-01795-5.
21. De Paepe B, De Bleecker JL. Cytokines and chemokines as regulators of skeletal muscle inflammation: presenting the case of Duchenne muscular dystrophy. *Mediat Inflamm*. 2013;2013, 540370. https://doi.org/10.1155/2013/540370.
22. Modi P, Shah BM, Patel S. Interleukin-1β converting enzyme (ICE): A comprehensive review on discovery and development of caspase-1 inhibitors. *Eur J Med Chem*. 2023;261, 115861. https://doi.org/10.1016/j.ejmech.2023.115861.
23. Li J, Hao JH, Yao D, et al. Caspase-1 inhibition prevents neuronal death by targeting the canonical inflammasome pathway of pyroptosis in a murine model of cerebral ischemia. *CNS Neurosci Ther*. 2020;26(9):925–939. https://doi.org/10.1111/cns.13384.
24. Cao DY, Zhang ZH, Li RZ, et al. A small molecule inhibitor of caspase-1 inhibits NLRP3 inflammasome activation and pyroptosis to alleviate gouty inflammation. *Immunol Lett*. 2022;244:28–39. https://doi.org/10.1016/j.imlet.2022.03.003.
25. Tang Y, Feng B, Wang Y, et al. Structure-based discovery of CZL80, a caspase-1 inhibitor with therapeutic potential for febrile seizures and later enhanced epileptogenic susceptibility. *Br J Pharmacol*. 2020;177(15):3519–3534. https://doi.org/10.1111/bph.15076.
26. Pan L, Tang WD, Wang K, et al. Novel Caspase-1 inhibitor CZL80 improves neurological function in mice after progressive ischemic stroke within a long therapeutic time-window. *Acta Pharmacol Sin*. 2022;43(11):2817–2827. https://doi.org/10.1038/s41401-022-00913-7.
27. Chen KP, Hua KF, Tsai FT, et al. A selective inhibitor of the NLRP3 inflammasome as a potential therapeutic approach for neuroprotection in a transgenic mouse model of Huntington's disease. *J Neuroinflammation*. 2022;19(1):56. https://doi.org/10.1186/s12974-022-02419-9.
28. Zhang X, Wang Z, Zheng Y, et al. Inhibitors of the NLRP3 inflammasome pathway as promising therapeutic candidates for inflammatory diseases (review). *Int J Mol Med*. 2023;51(4):35. https://doi.org/10.3892/ijmm.2023.5238.
29. Dhani S, Zhao Y, Zhivotovsky B. A long way to go: caspase inhibitors in clinical use. *Cell Death Dis*. 2021;12(10):949. https://doi.org/10.1038/s41419-021-04240-3.
30. Löser R, Abbenante G, Madala PK, Halili M, Le GT, Fairlie DP. Noncovalent Tripeptidyl benzyl- and Cyclohexyl-amine inhibitors of the cysteine protease Caspase-1. *J Med Chem*. 2010;53(6):2651–2655. https://doi.org/10.1021/jm901790w.
31. Poreba M, Szalek A, Kasperkiewicz P, Rut W, Salvesen GS, Drag M. Small molecule active site directed tools for studying human caspases. *Chem Rev*. 2015;115(22):12546–12629. https://doi.org/10.1021/acs.chemrev.5b00434.
32. Kitchen DB, Decornez H, Furr JR, Bajorath J. Docking and scoring in virtual screening for drug discovery: methods and applications. *Nat Rev Drug Discov*. 2004;3(11):935–949. https://doi.org/10.1038/nrd1549.
33. De Vivo M, Masetti M, Bottegoni G, Cavalli A. Role of molecular dynamics and related methods in drug discovery. *J Med Chem*. 2016;59(9):4035–4061. https://doi.org/10.1021/acs.jmedchem.5b01684.
34.. Jumper J, Evans R, Pritzel A, et al. Highly accurate protein structure prediction with AlphaFold. *Nature*. 2021;596:583–589. https://doi.org/10.1038/s41586-021-03819-2.
35. Ulgheri F, Spanu P, Deligia F, et al. Design, synthesis and biological evaluation of 1,5-disubstituted α-amino tetrazole derivatives as non-covalent inflammasome-caspase-1 complex inhibitors with potential application against immune and inflammatory disorders. *Eur J Med Chem*. 2022;229, 114002. https://doi.org/10.1016/j.ejmech.2021.114002.
36.. Alexander Domling, Pietro Spanu, and Fausta Ulgheri are co-inventors of patent application EP3666769A1 ("Novel Caspase Inhibitors"), which included compounds related to the present study. The patent application was subsequently withdrawn and is not currently in force.
37. Fournier JF, Clary L, Chambon S, et al. Rational drug Design of Topically Administered Caspase 1 inhibitors for the treatment of inflammatory acne. *J Med Chem*. 2018;61(9):4030–4051. https://doi.org/10.1021/acs.jmedchem.8b00067.
38. Neochoritis CG, Zhao T, Dömling A. Tetrazoles via Multicomponent Reactions. *Chem Rev*. 2019;119(3):1970–2042. https://doi.org/10.1021/acs.chemrev.8b00564.
39. Chandgude AL, Dömling A. An efficient Passerini tetrazole reaction (PT-3CR). *Green Chem*. 2016;18(13):3718–3721. https://doi.org/10.1039/c6gc00910g.
40. Zhao T, Kurpiewska K, Kalinowska-Tłuścik J, Herdtweck E, Dömling A. α-Amino acid-isosteric α-amino tetrazoles. *Chem Eur J*. 2016;22(9):3009–3018. https://doi.org/10.1002/chem.201504520.
41. Lei X, Lampiri P, Patil P, Angeli G, Neochoritis CG, Dömling A. A multicomponent tetrazolo indole synthesis. *Chem Commun*. 2021;57(54):6652–6655. https://doi.org/10.1039/d1cc02384e.
42.. Only a Free-Wilson analysis of one tetrazole derivative as covalent caspase-1 inhibitors was reported. See ref. 35.
43. Iannotti FA, Pagano E, Guardiola O, et al. Genetic and pharmacological regulation of the endocannabinoid CB1 receptor in Duchenne muscular dystrophy. *Nat Commun*. 2018;9(1):3950. https://doi.org/10.1038/s41467-018-06267-1.
44. Li J, Chandgude AL, Zheng Q, Dömling A. Innovative synthesis of drug-like molecules using tetrazole as core building blocks. *Beilstein Arch*. 2024, 20247. https://doi.org/10.3762/bxiv.2024.7.v1.
45. Dömling A, Wang W, Wang K. Chemistry and biology of multicomponent reactions. *Chem Rev*. 2012;112(6):3083–3135. https://doi.org/10.1021/cr100233r.
46. McNutt AT, Francoeur P, Aggarwal R, et al. GNINA 1.0: molecular docking with deep learning. *J Cheminform*. 2021;13(1), 43. https://doi.org/10.1186/s13321-021-00522-2.
47. Wu M, Li H, He J, Liang J, Liu Y, Zhang W. TRIM72 alleviates muscle inflammation in mdx mice via promoting mitophagy-mediated NLRP3 inflammasome inactivation. *Oxidative Med Cell Longev*. 2023;2023, 8408574. https://doi.org/10.1155/2023/8408574.
48. Lau YS, Zhao L, Zhang C, Li H, Han R. Genetic disruption of the inflammasome adaptor ASC has minimal impact on the pathogenesis of Duchenne muscular dystrophy in mdx mice. *Life Sci*. 2020;257, 118069. https://doi.org/10.1016/j.lfs.2020.118069.
49. Singh V, Ubaid S, Kashif M, et al. Role of inflammasomes in cancer immunity: mechanisms and therapeutic potential. *J Exp Clin Cancer Res*. 2025;44(1):109. https://doi.org/10.1186/s13046-025-03366-y.
50. Denes A, Lopez-Castejon G, Brough D. Caspase-1: is IL-1 just the tip of the ICEberg? *Cell Death Dis*. 2012;3(7), e338. https://doi.org/10.1038/cddis.2012.86.
51. Antuña E, Potes Y, Baena-Huerta FJ, et al. NLRP3 contributes to sarcopenia associated to dependency recapitulating inflammatory-associated muscle degeneration. *Int J Mol Sci*. 2024;25(3):1439. https://doi.org/10.3390/ijms25031439.
52. Kalkan H, Pagano E, Paris D, et al. Targeting gut dysbiosis against inflammation and impaired autophagy in Duchenne muscular dystrophy. *EMBO Mol Med*. 2023;15(3), e16225. https://doi.org/10.15252/emmm.202216225.
53. Xu X, Wang J, Wang M, et al. Structure-enabled discovery of novel macrocyclic inhibitors targeting Glutaminase 1 allosteric binding site. *J Med Chem*. 2021;64(8):4588–4611. https://doi.org/10.1021/acs.jmedchem.0c02044.
54. Zhu P, Yang Y, Qian J, et al. Discovery of novel thiophene[2,3-d]pyrimidine-thiazole derivative as a promising MNK inhibitor to treat breast cancer. *J Mol Struct*. 2025;1321:14012. https://doi.org/10.1016/j.molstruc.2024.140125.
55. Bouysset C, Fiorucci S. ProLIF: a library to encode molecular interactions as fingerprints. *J Cheminform*. 2021;13(1):72. https://doi.org/10.1186/s13321-021-00548-6.
56. Gerber PR, Müller K. MAB, a generally applicable molecular force field for structure modelling in medicinal chemistry. *J Comput Aided Mol Des*. 1995;9(3):251–268. https://doi.org/10.1007/BF00124456.
57. Kalkan H, Panza E, Pagano E, et al. Dysfunctional endocannabinoid CB1 receptor expression and signaling contribute to skeletal muscle cell toxicity induced by simvastatin. *Cell Death Dis*. 2023;14(8):544. https://doi.org/10.1038/s41419-023-06080-9.